



Resilience of the Aurivillius structure upon La and Cr doping in Bi₅Ti₃FeO₁₅ multiferroic

Journal:	<i>Dalton Transactions</i>
Manuscript ID	DT-ART-01-2024-000159.R1
Article Type:	Paper
Date Submitted by the Author:	19-Feb-2024
Complete List of Authors:	Salas Correa, Omar; The University of Texas at El Paso, Department of Physics Getahun, Yohannes W.; The University of Texas at El Paso Mandujano, Hector; The University of Texas at El Paso, Department of Physics Manciu, F. S.; The University of Texas at El Paso Castellanos, Mariana; The University of Texas at El Paso, Department of Physics Lopez, Jorge ; University of Texas at El Paso, Physics Garza-Hernández, Raquel ; Centro de Investigaciones en Optica AC, Energy Buturlim, Volodymyr; Idaho National Laboratory, Glenn T. Seaborg Institute Gofryk, Krzysztof; Idaho National Laboratory Bairwa, Dhanpal; Indian Institute of Science Elizabeth, Suja; Indian Institute of Science, Bangalore, Physics Nair, Harikrishnan; The University of Texas at El Paso, Department of Physics



Cite this: DOI: 10.1039/xxxxxxxxxx

Resilience of the Aurivillius structure upon La and Cr doping in $\text{Bi}_5\text{Ti}_3\text{FeO}_{15}$ multiferroic.

Omar Alejandro Salas,^a Yohannes W. Getahun,^a Cein H. Mandujano,^b Felicia Manciu,^a Mariana Castellanos,^a Jorge Lopez,^a Raquel Garza Hernández,^c Volodymir B. Buturlim,^d Krzysztof Gofryk,^e Dhanpal Bairwa,^f Suja Elizabeth,^f and Harikrishnan S. Nair,^a

Received Date
Accepted Date

DOI: 10.1039/xxxxxxxxxx

www.rsc.org/journalname

Combining the experimental techniques of high-resolution X-ray diffraction, magnetometry, specific heat, and X-ray photoelectron, Raman and dielectric spectroscopies, we have studied the influence of La and Cr doping on the crystal structure and magnetism of the room temperature Aurivillius multiferroic $\text{Bi}_5\text{Ti}_3\text{FeO}_{15}$ by investigating the physical properties of $(\text{Bi}_4\text{La})\text{Ti}_3\text{FeO}_{15}$ and $\text{Bi}_5\text{Ti}_3(\text{Fe}_{0.5}\text{Cr}_{0.5})\text{O}_{15}$. The parent ($\text{Bi}_5\text{Ti}_3\text{FeO}_{15}$) and the doped ($(\text{Bi}_4\text{La})\text{Ti}_3\text{FeO}_{15}$, $\text{Bi}_5\text{Ti}_3(\text{Fe}_{0.5}\text{Cr}_{0.5})\text{O}_{15}$) compounds crystallize in $A2_1am$ space group, which is confirmed through our analysis of high-resolution synchrotron X-ray diffraction data obtained on phase-pure polycrystalline powders. We determined the oxidation states of the metal atoms in the studied compounds as Fe^{+3} , Ti^{+4} , Cr^{+3} and La^{+3} through the analysis of X-ray photoelectron spectroscopy data. The magnetic susceptibilities of the three compounds are marked by the absence of a long-range ordered ground state, but dominated by superparamagnetic clusters with dominant antiferromagnetic interactions. This signature of short-range magnetism is also seen in specific heat as a low temperature enhancement which is suppressed upon the application of external magnetic fields upto 8 T. Our dielectric spectroscopy experiments showed that the three studied compounds display similar features in dielectric constant measured as a function of frequency. However, upon doping La at Bi site, the width of the ferroelectric hysteresis loop increases for $(\text{Bi}_4\text{La})\text{Ti}_3\text{FeO}_{15}$, compared to that of the parent compound $\text{Bi}_5\text{Ti}_3\text{FeO}_{15}$; and with Cr-doping, $\text{Bi}_5\text{Ti}_3(\text{Fe}_{0.5}\text{Cr}_{0.5})\text{O}_{15}$ becomes a leaky dielectric. The resilience of the Aurivillius crystal structure towards doping of La at Bi site and Cr at Fe site is clearly seen in the bulk properties of magnetic susceptibility, specific heat and average crystal structure. The relevance of changes in the local structure is evident from our Raman spectroscopy and X-ray pair distribution function studies.

1 Introduction

Efficient and sustainable data and energy storage materials are essential requirements of modern societies. Environmental friendly

^a Department of Physics, 500 W University Ave, The University of Texas at El Paso, El Paso, TX 79968, USA. Fax: 91 5747 5447; Tel: 91 5747 7544; E-mail: hnair@utep.edu

^b Department of Chemistry and Biochemistry, University of Maryland, College Park, Maryland, MD 20742, USA.

^c Centro de Investigaciones en Óptica A.C., León, Guanajuato, Mexico.

^d Glenn T. Seaborg Institute, Idaho National Laboratory, Idaho Falls, ID 83415, USA.

^e Center for Quantum Actinide Science and Technology, Idaho National Laboratory, Idaho National Laboratory, Idaho Falls, ID 83415, USA.

^f Department of Physics, Indian Institute of Science, Bangalore, 560012, India.

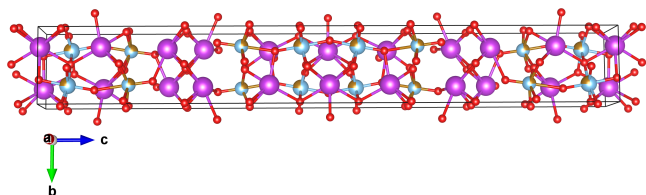


Fig. 1 A schematic of the crystal structure of the Aurivillius perovskite $\text{Bi}_5\text{Ti}_3\text{FeO}_{15}$, crystallizing in $A2_1am$ space group. The large purple spheres are Bi atoms and the red small spheres are oxygen. The c axis is approximately 41 Å long.

materials are actively researched for most technological applications we use today on a regular basis. Aurivillius perovskites are layered structures which fit the bill for sustainable data and energy storage applications. On the one hand, they are actively researched in the fields of condensed matter physics, materials science, and engineering as single phase multiferroics. These are materials which combine switchable electric and magnetic polarizations^{1–5}. A desirable outcome of research in this area will be the discovery of a room temperature multiferroic which has strong coupling between the electric and magnetic polarizations, and very low leakage. BiFeO_3 is a well-known material which is reported to show large spontaneous polarization and G-type antiferromagnetic order above room temperature⁶. However, leakage and defects hampered its practical applications. Discovery and optimization of single phase multiferroic materials operating at or near room temperature is a challenge. Perovskite compounds with a layered crystal structure are highly desirable in this respect due to the possibility that their crystal structures offer for inserting magnetic or ferroelectric entities as desired, to make the material multiferroic. A strong candidate is the Aurivillius family of compounds⁷.

$\text{Bi}_4\text{Ti}_3\text{O}_{12}$ -derived compounds have propitious perovskite blocks sandwiched between Bi_2O_2 layers with additional advantages that the bismuth oxide layers will act as a reservoir for oxygen ions, and also as an insulating layer to prevent charge hopping^{8,9}. Insertion of BiFeO_3 motifs into $\text{Bi}_4\text{Ti}_3\text{O}_{12}$ showed that the resulting compound was multiferroic at room temperature^{10–12}. The Aurivillius crystal structure offers the possibility to tune the number of layers, doping at the bismuth as well as the transition metal atom sites to tune the structure, ferroelectric and magnetic properties, thereby offering a large tunable parameter space for multiferroic properties^{7,13,14}. The Aurivillius compounds have the general formula $\text{Bi}_{n+1}\text{Fe}_{n-3}\text{Ti}_3\text{O}_{3n+3}$ ($\text{BFTO}-n$). For integer value of n , compounds such as $\text{Bi}_5\text{FeTi}_3\text{O}_{15}$, $\text{Bi}_6\text{Fe}_2\text{Ti}_3\text{O}_{18}$, and $\text{Bi}_7\text{Fe}_3\text{Ti}_3\text{O}_{21}$ have been studied^{15–17}. Aurivillius compounds with n upto 9 have been synthesized using different methods, whereas compounds with $n > 9$ tend to form impurity phases¹⁸. Compounds with fractional n also exist, in which case, perovskite layers of different thicknesses alternate in the compound. In addition to controlling the layer number and thickness, properties of Aurivillius perovskites can be tuned by chemical doping at the transition metal site. For example, enhanced ferromagnetism was observed upon half substitution of Fe^{3+} by Co^{3+} in $\text{Bi}_5\text{Ti}_3\text{FeO}_{15}$ because of the ferromagnetic interaction between adjacent Fe^{3+}

	a (Å)	b (Å)	c (Å)	V (Å) ³	δ	χ^2
BTFO	5.4690(1)	5.4397(8)	41.2496(2)	1227.18(3)	0.0026	2.67
BTFCO	5.4620(3)	5.4402(6)	40.9672(7)	1217.33(5)	0.0019	1.59
BLTFO	5.4491(1)	5.4456(2)	41.3155(1)	1226.06(7)	0.0004	4.06

Table 1 The lattice parameters, cell volume, distortion index δ and the goodness-of-fit (χ^2) obtained from Rietveld refinement of the synchrotron diffraction patterns measured at the Canadian Light Source.

and Co^{3+} ions^{19–21}.

$\text{Bi}_5\text{Ti}_3\text{FeO}_{15}$ is a promising member in the Aurivillius family that shows a wide variety of physical properties including magnetoelectric effect²², high-temperature ferroelectricity²³, and a piezoelectric coefficient of 35.28 pm/V²⁴. $\text{Bi}_5\text{Ti}_3\text{FeO}_{15}$ also exhibits appreciable optical properties^{25–27}. The number of perovskite layers play an important role in the crystal structure and thereby influence the physical properties of $\text{Bi}_5\text{Ti}_3\text{FeO}_{15}$ and related compounds. This four-layered multiferroic has been reported in three different space groups, $A2_1am$, $Fmm2$ and $Pnn2$ ^{28–30}. The assignment of the space group $Fmm2$ was made on a twinned single crystal of $\text{Bi}_5\text{Ti}_3\text{FeO}_{15}$ grown using high temperature method employing $\text{Bi}_2\text{O}_3/\text{B}_2\text{O}_3$ flux²⁸. The assignment of the space group $A2_1am$ was using diffraction data on powder samples of $\text{Bi}_5\text{Ti}_3\text{FeO}_{15}$ obtained using solid state synthesis conducted at 1000°C²⁹. The samples on which $Pnn2$ space group is reported was also prepared using solid state route, but using a slightly different synthesis temperature of 1050°C³⁰. The inconsistency in the space group assignment of the parent compound, $\text{Bi}_5\text{Ti}_3\text{FeO}_{15}$, was resolved in an electron diffraction study which finally assigned the space group as $A2_1am$ ³¹. There seem to be only slight differences in the synthesis parameters reported by different groups for this material. Hence, as inferred correctly in Zheng *et al*, the main reason for the space group discrepancy is due to poor resolution of diffraction data.

Even-layered Aurivillius compounds show a structural phase transition from ferroelectric $A2_1am$ to paraelectric tetragonal $I4/mmm$. This was found to be the case of $\text{Bi}_5\text{Ti}_3\text{FeO}_{15}$, studied using high-temperature neutron powder diffraction^{32,33}. Since the primary structural motif of the Aurivillius compounds is the network of octahedra, it is possible to tune the physical properties through cation displacements and octahedral rotations. This can be achieved by applying external pressure or by modifying crystal structure through chemical pressure. The parent compound $\text{Bi}_5\text{Ti}_3\text{FeO}_{15}$ is a good ferroelectric with a Curie temperature close to 750°C, however, its magnetism is not conclusively understood. Doping Co in $\text{Bi}_5\text{Ti}_3\text{FeO}_{15}$ is reported to improve the magnetoelectric coefficient to a value of 11.47 mV cm⁻¹Oe⁻¹³⁴. This is attributed to the structural distortion caused by Co substitution which subsequently leads to ferromagnetic interactions via the Dzyaloshinskii-Moriya interaction. Doping the Ti site with multiple ions is also reported to enhance the multiferroic properties, for example, $\text{Bi}_5\text{FeTi}_2\text{Nb}_{0.5}\text{Co}_{0.5}\text{O}_{15}$ is reported to show superior values of remnant magnetization and polarization of 76.4 memu/g and 10.2 $\mu\text{C}/\text{cm}^2$ ³⁵. Similar effect is brought out by doping Ni in the place of Fe in $\text{Bi}_5\text{Ti}_3\text{FeO}_{15}$. In $\text{Bi}_5\text{Ti}_3\text{Fe}_{0.5}\text{Ni}_{0.5}\text{O}_{15}$, the fer-

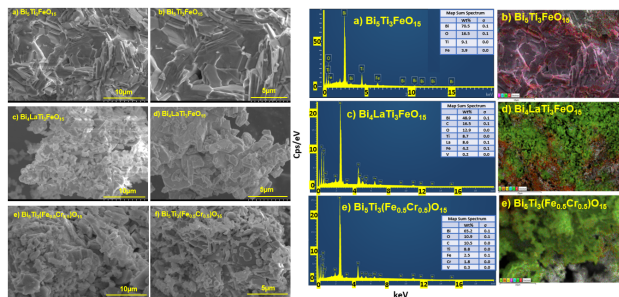


Fig. 2 Scanning electron micrograph images of $\text{Bi}_5\text{Ti}_3\text{FeO}_{15}$ at (a) 10 μm and (b) 5 μm , $(\text{Bi}_4\text{La})\text{Ti}_3\text{FeO}_{15}$ at (e) 10 μm and (f) 5 μm , and $\text{Bi}_5\text{Ti}_3(\text{Fe}_{0.5}\text{Cr}_{0.5})\text{O}_{15}$ at (i) 10 μm and (j) 5 μm . Energy-dispersive X-ray micrographs and elemental mapping for $\text{Bi}_5\text{Ti}_3\text{FeO}_{15}$, (c) and (d); for $(\text{Bi}_4\text{La})\text{Ti}_3\text{FeO}_{15}$, (g) and (h) and for $\text{Bi}_5\text{Ti}_3(\text{Fe}_{0.5}\text{Cr}_{0.5})\text{O}_{15}$, (k) and (l) respectively.

roelectric and magnetic Curie temperatures are 1100 K and 726 K. The room temperature multiferroic behavior of this compound was demonstrated by the ferroelectric polarization of $8.5 \mu\text{C}/\text{cm}^2$ and remnant magnetization of 27.86 m emu/g³⁶. Once again, these properties were attributed to the Dzyaloshinskii-Moriya interaction. The compositional tunability of the Aurivillius compounds is displayed by $\text{Bi}_{3.25}\text{La}_{0.75}\text{Ti}_{2.5}\text{Nb}_{0.25}(\text{Fe}_{0.5}\text{Co}_{0.5})_{0.25}\text{O}_{12}$ which is a single phase compound and a room temperature multiferroic³⁷. Direct visualization of magnetic field induced magnetoelectric coupling in thin films of $\text{Bi}_6\text{Ti}_{2.8}\text{Fe}_{1.52}\text{Mn}_{0.68}\text{O}_{18}$ ³⁸ shows how complex structure and composition in Aurivillius compounds lead to multiferroicity.

Energy storage is another important application potential of Aurivillius compounds which are reported to possess unmatched fatigue resistance. This useful feature is due to the layered architecture of the compound that acts as barriers to inhibit long-range diffusion of space charges and defects^{39,40}. High-energy density dielectric capacitors are one promising field where Aurivillius perovskites can find application, but are currently less explored⁴¹. Composition modification of $\text{Bi}_{3.25}\text{La}_{0.75}\text{Ti}_3\text{O}_{12}$ with BiFeO_3 is reported to reduce leakage currents and improve breakdown strength, thereby promising better ceramic capacitors⁴². Energy storage potential of thin films of Aurivillius compounds is very promising. For instance, films of Nd-doped $\text{Bi}_4\text{Ti}_3\text{O}_{12}$ have an energy storage density of $41.6 \text{ J}\cdot\text{cm}^{-3}$ with an efficiency of 84.3% under $2300 \text{ kV}/\text{cm}^2$ ⁴³. Energy storage density of films of $\text{BaBi}_4\text{Ti}_4\text{O}_{15}$ can reach $37.7 \text{ J}\cdot\text{cm}^{-3}$ with an efficiency of more than 80% under $2000 \text{ kV}/\text{cm}^2$ ⁴⁴. The Aurivillius compounds are ideal candidates for energy storage applications because they are poison-free and pollution-free. Their crystal structure can be easily intercalated^{45,46}. The ferroelectric ground state of these compounds are highly sensitive to intercalation units which influence electrocaloric, energy storage, and energy sensor applications^{47–49}. In principle, the ferroelectric domain patterns are favorable to form polar nanoregion, which are driven by gradient of elastic energy and dipole interaction. The nano-domain patterns are the source of the high energy storage behavior^{50,51}.

In the present work, we have chemically modified $\text{Bi}_5\text{Ti}_3\text{FeO}_{15}$ by substituting La at the Bi site, and Cr at the Fe site, to create

$(\text{Bi}_4\text{La})\text{Ti}_3\text{FeO}_{15}$ and $\text{Bi}_5\text{Ti}_3(\text{Fe}_{0.5}\text{Cr}_{0.5})\text{O}_{15}$ with the aim of introducing ionic size differences such that the ferroelectric and magnetic characteristics are improved. We present the results of magnetic, dielectric and thermodynamic experiments and microscopic structural features of the three Aurivillius compounds studied in this work.

2 Experimental methods

The Aurivillius compounds studied in this work were prepared using standard solid state synthesis methods. The oxides, Bi_2O_3 , Fe_2O_3 , TiO_2 , La_2O_3 , and Cr_2O_3 (of purity 4N or higher) were used as reactants and were mixed in stoichiometric ratios of $\text{Bi}_5\text{Ti}_3\text{FeO}_{15}$, $(\text{Bi}_4\text{La})\text{Ti}_3\text{FeO}_{15}$, and $\text{Bi}_5\text{Ti}_3(\text{Fe}_{0.5}\text{Cr}_{0.5})\text{O}_{15}$ for synthesis. After thoroughly mixing the reactants, each sample was ground, pressed into a pellet and heated at $1050 \text{ }^\circ\text{C}$ for two hours. The process of heating and pelleting was repeated a few times, with intermediate grinding. After synthesis, the pellets were ground and used for laboratory powder X-ray diffraction (PXRD) using a Panalytical Empyrean diffractometer operated with a Cu-target ($\lambda = 1.540 \text{ \AA}$).

We performed high resolution synchrotron X-ray diffraction using these samples to characterize the crystal structures of the three compounds. The experiments were performed at 295 K at the BXDS beamline of the Canadian Light Source (CLS) using a wavelength of 0.2038 \AA . General Structure Analysis Software (GSAS-II)⁵² was used for the analysis of the diffraction data presented in this work. Total scattering data with a $Q_{\text{max}} = 25 \text{ \AA}^{-1}$ was also collected at the BXDS beamline, using $\lambda = 0.2038 \text{ \AA}$. Pair distribution function (PDF) analysis of the data was carried out using the software, PDFgui⁵³.

We investigated the morphology of the samples using Hitachi S-4800 Field Emission Scanning Electron Microscope (FE-SEM) detector type XFlash 6-60 ex, equipped with energy dispersive X-ray (EDX) option from Bruker Nano GmbH Berlin, Germany at different resolutions. Elemental mapping was simultaneously conducted for high resolution images on the same SEM machine. The heat capacity and magnetic susceptibility as a function of temperature and isothermal magnetization as a function of magnetic field of the three compounds were measured using a Physical Property Measurement System (DynaCool PPMS) in zero and applied magnetic fields upto 10 T.

The X-ray photoelectron spectroscopy (XPS) analyses were carried out in a PerkinElmer PHI 5600 spectrometer with a hemispherical energy analyzer, using magnesium ($\text{Al K}\alpha$) source of 1486.7 eV at 100 Watts. The pressure in the analysis chamber during XPS analysis was in the low range of 10^{-9} Torr. All spectra were recorded at 54° take off angle, the analyzed area being currently about 1 mm^2 . All spectra were recorded with 0.25 eV step and corrected using carbon signal (C_{1s}) at 284.8 eV. XPS spectra were analyzed with Analyzer software using the Shirley method for removing the background necessary for curve fitting.

The Raman scattering data were acquired at ambient conditions in backscattering geometry with an alpha 300R WITec system (WITec GmbH, Ulm, Germany). A 532 nm excitation of a frequency-doubled neodymium doped yttrium aluminum garnet (Nd YAG) laser restricted to a power output of a few mW and a

20x objective lens with a numerical aperture of 0.4 were used. The accumulation of data for each sample consisted of 20 Raman spectra, with each spectrum acquired in 500 milliseconds, for a total time acquisition of 10 seconds. The spectral resolution was 4 cm^{-1} . Appropriate background subtractions were performed for the fitted Raman spectra.

Ferroelectric loop measurements were conducted on polycrystalline pellets with a density of around 95% and a thickness below 0.5 mm. Silver paint was applied to both sides of the pellets to facilitate the measurements, which were carried out using Precision Ferroelectric loop-tester. Frequency-dependent impedance measurements were carried out using Agilent 4294a impedance analyzer in the frequency range, 100 Hz and 107 Hz, at various temperatures between 305 K and 500 K.

3 Results and discussion

3.1 Elemental characterization

Figure 2 shows the micrography (SEM-EDX) results, where the morphology of (a, b) $\text{Bi}_5\text{Ti}_3\text{FeO}_{15}$ (e, f) $(\text{Bi}_4\text{La})\text{Ti}_3\text{FeO}_{15}$ and (i, j) $\text{Bi}_5\text{Ti}_3(\text{Fe}_{0.5}\text{Cr}_{0.5})\text{O}_{15}$ and the elemental information presented in (c, d) for $\text{Bi}_5\text{Ti}_3\text{FeO}_{15}$, (g, h) for $(\text{Bi}_4\text{La})\text{Ti}_3\text{FeO}_{15}$, and (k, l) for $\text{Bi}_5\text{Ti}_3(\text{Fe}_{0.5}\text{Cr}_{0.5})\text{O}_{15}$. The observed sheet-like grain structure and disordered arrangement are characteristic of the present multiferroic ceramic material, in agreement with previous reports^{54–56}. The difference in grain shape after doping with either La or Cr suggests a discernible impact of these atoms on crystal growth of the parent compound, $\text{Bi}_5\text{Ti}_3\text{FeO}_{15}$. The pristine $\text{Bi}_5\text{Ti}_3\text{FeO}_{15}$ compound displayed uniform and dense microstructure demonstrating substantial grain growth, oriented perpendicular to the *c*-axis. Upon the introduction of La or Cr into the crystal structure, a transformation is observed, resulting in a composite of sheet like grains and finely textured particles. Since all samples were synthesized under the same temperature conditions, this adaptation could be attributed to variances in growth kinetic patterns induced upon the introduction of doping elements. La ion possesses complex electronic structure with partially filled *f*-orbitals, which imparts a propensity for strong interaction with neighboring atoms and the potential to occupy certain lattice sites due to their size and charge characteristics. These attributes may facilitate their diffusion throughout the crystal which eventually impedes the crystal growth in the parent compound^{25,57}. Alteration of grain morphology in five-layered Aurivillius $\text{Bi}_6\text{Fe}_2\text{Ti}_3\text{O}_{18}$ upon La and Co substitution is reported¹⁶. Chromium ions can interfere with the crystal lattice involving the occupation of lattice sites replacing other metal ions or diffuse to defect locations primarily attributed to their relatively smaller size and charge⁵⁸. Particularly, the comparable size and charge of chromium ions (+3) with the charge of iron makes it compatible. Therefore, the impact on the crystal structure of $\text{Bi}_5\text{Ti}_3\text{FeO}_{15}$ is possibly resulting from external factors such as electric field and chemical gradients. Effective incorporation of La and Cr into the target Aurivillius compound is substantiated through the examination of our EDX data. The weight percentages of each element closely align with their expected stoichiometric concentrations established during the synthesis process. The elemental distribution of $\text{Bi}_5\text{Ti}_3\text{FeO}_{15}$,

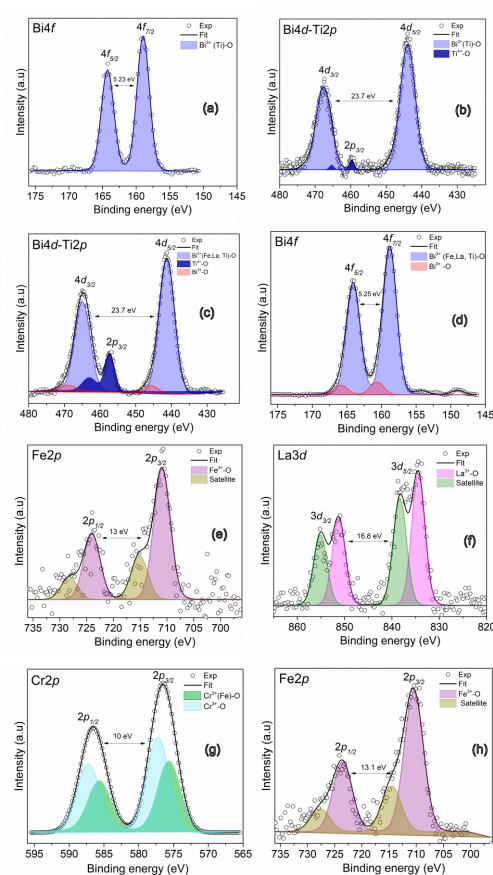


Fig. 3 The X-ray photoelectron spectra of (a, b) $\text{Bi}_5\text{Ti}_3\text{FeO}_{15}$, (c-f) $(\text{Bi}_4\text{La})\text{Ti}_3\text{FeO}_{15}$ and (g, h) $\text{Bi}_5\text{Ti}_3(\text{Fe}_{0.5}\text{Cr}_{0.5})\text{O}_{15}$. Solid lines are profile fits to the experimental data, shown in circles.

as depicted in Figure 2 and the spatial composition mapping, illustrate the successful diffusion of La and Cr. A uniform and dense distribution of elements within $\text{Bi}_5\text{Ti}_3\text{FeO}_{15}$, is supported by our SEM data. Minimal vanadium impurities were detected, with the observed carbon content attributed to the utilization of carbon tape for securing the sample.

The XPS data for the three compounds $\text{Bi}_5\text{Ti}_3\text{FeO}_{15}$, $(\text{Bi}_4\text{La})\text{Ti}_3\text{FeO}_{15}$ and $\text{Bi}_5\text{Ti}_3(\text{Fe}_{0.5}\text{Cr}_{0.5})\text{O}_{15}$ are shown in Figure 3. The data and profile fits for $\text{Bi}_5\text{Ti}_3\text{FeO}_{15}$ are shown in (a, b) panels of the figure. The Bi $4f_{7/2}$ peak at 159.015 eV and the Bi $4f_{5/2}$ peak at 164.25 eV are consistent with Bi(III) in oxide or oxohalide compounds. The Bi $4d_{5/2}$ peak at 443.96 eV and the Bi $4d_{3/2}$ peak at 467.62 eV are also consistent with Bi(III) oxidation state. The Ti $2p_{3/2}$ and Ti $2p_{1/2}$ peaks at 459.64 eV and 465.34 eV are consistent with Ti(IV) in oxide compounds. The XPS analysis was inconclusive in determining the presence or oxidation state of Fe, since no Fe core level peaks are visible. This might be attributed to a lack of intensity, which in turn might be caused by the attenuation of the other metals at the surface. Therefore, the oxidation states of the elements in this XPS spectra are: Bi(III) and Ti(IV).

The experimental XPS spectra and the curve fits of $(\text{Bi}_4\text{La})\text{Ti}_3\text{FeO}_{15}$ are shown in the panels (c-f) in the figure. The Bi $4f_{7/2}$ peak at 158.83 eV and the Bi $4f_{5/2}$ peak at 164.129 eV are consistent with Bi(III) in oxide or oxohalide compounds. The Ti

$2p_{3/2}$ and Ti $2p_{1/2}$ peaks at 457.32 eV and 463.04 eV are consistent with Ti(IV) in oxide compounds. The Fe $2p_{3/2}$ peak at 710.96 eV and the Fe $2p_{1/2}$ peak at 724 eV are consistent with Fe(III) in oxide compounds. The Fe $2p$ peaks for Fe(III) are typically found at higher binding energies than those for Fe(II). Specifically, the Fe $2p_{3/2}$ peak for Fe(III) is usually found in the range of 710-713 eV, while the Fe $2p_{1/2}$ peak is usually found in the range of 723-727 eV. The Fe $2p_{3/2}$ peak for Fe(II), on the other hand, is typically found at a lower binding energy, in the range of 705-709 eV, with the Fe $2p_{1/2}$ peak at 718-722 eV. The La $3d_{3/2}$ peak at 854.6 eV and the La $3d_{5/2}$ peak at 835.4 eV are consistent with La(III) in oxide compounds. Therefore, the oxidation states of the elements in this XPS spectra are: Bi(III), Ti(IV), Fe(III), and La(III).

The XPS spectra of $\text{Bi}_5\text{Ti}_3(\text{Fe}_{0.5}\text{Cr}_{0.5})\text{O}_{15}$ are shown in panels (g, h) in Figure 3. The Bi $4f_{7/2}$ peak at 152.6 eV and the Bi $4f_{5/2}$ peak at 168.1 eV are consistent with Bi(III) in oxide or oxohalide compounds. The Bi $4d_{5/2}$ peaks at 444.2 eV and the Bi $4d_{3/2}$ peak at 451.8 eV are also consistent with Bi(III) oxidation state. The XPS analysis was inconclusive in determining the presence of Ti. However, Ti is typically found in the +4 oxidation state in oxides, so it is reasonable to assume that Ti, if present in $\text{Bi}_5\text{Ti}_3(\text{Fe}_{0.5}\text{Cr}_{0.5})\text{O}_{15}$, is also in the +4 oxidation state. The Fe $2p_{3/2}$ peak at 710.48 eV and the Fe $2p_{1/2}$ peak at 723.61 eV are consistent with Fe(III) in oxide compounds. The Cr $2p_{3/2}$ peak at 575.59 eV and the Cr $2p_{1/2}$ peak at 585.65 eV are consistent with Cr(III) oxidation state. Therefore, the oxidation states of the elements in this XPS spectra are: Bi(III), Fe(III), and Cr(III).

3.2 Crystal structure

The details of the crystal structures of the three Aurivillius perovskites, $\text{Bi}_5\text{Ti}_3\text{FeO}_{15}$ (BTFO), $(\text{Bi}_4\text{La})\text{Ti}_3\text{FeO}_{15}$ (BLTFO) and $\text{Bi}_5\text{Ti}_3(\text{Fe}_{0.5}\text{Cr}_{0.5})\text{O}_{15}$ (BTFCO), studied in this work are obtained through Rietveld analysis⁵⁹ of the diffraction data measured at the synchrotron beamline BXDS at CLS. The experimental data along with the refinements are shown in Figure 4. The reflections of $\text{Bi}_5\text{Ti}_3\text{FeO}_{15}$, $(\text{Bi}_4\text{La})\text{Ti}_3\text{FeO}_{15}$ and $\text{Bi}_5\text{Ti}_3(\text{Fe}_{0.5}\text{Cr}_{0.5})\text{O}_{15}$, closely match the structure reported for $\text{Bi}_5\text{Ti}_3\text{FeO}_{15}$ ²⁹.

We found that the space group $A2_1am$ offers the best description of the experimental reflections. Rietveld analysis of the experimental synchrotron X-ray diffraction data was hence undertaken using this space group model. The refined lattice parameters for the three compositions obtained from this analysis are presented in Table 1. An earlier work²⁸ described the crystal structure of $\text{Bi}_5\text{Ti}_3\text{FeO}_{15}$ using a different space group, $Fmm2$, following experiments performed on single crystals. They reported the lattice parameters as $a(\text{\AA}) = 5.4318(6)$, $b(\text{\AA}) = 41.149(4)$ and $c(\text{\AA}) = 5.4691(12)$. In the present work, the effect of doping La^{3+} into Bi site leads to an increase in the lattice constant c from 41.1732(2) to 41.2475(0). As a result of the expansion of the unit cell, the cell volume increases to 1226.78(7) (\AA^3). This behaviour in $(\text{Bi}_4\text{La})\text{Ti}_3\text{FeO}_{15}$ is different from what is reported for Gd-doping at the Bi site of $\text{Bi}_5\text{Ti}_3\text{FeO}_{15}$ ¹⁵. An index of distortion is defined for the Aurivillius compounds as $\delta = \frac{2(a-b)}{a+b}$. It can be seen from the δ values in Table 1 that the average distortion is high in the parent compound than in the doped variants, be it La

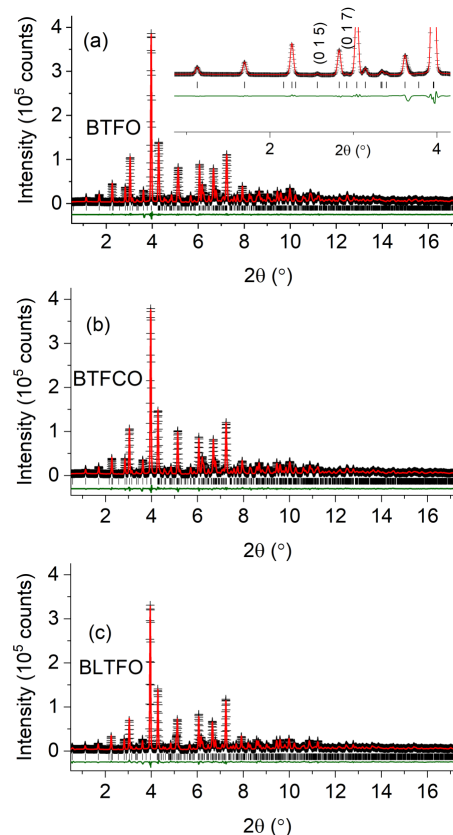


Fig. 4 The synchrotron X-ray diffraction patterns of (a) $\text{Bi}_5\text{Ti}_3\text{FeO}_{15}$ (b) $(\text{Bi}_4\text{La})\text{Ti}_3\text{FeO}_{15}$ and (c) $\text{Bi}_5\text{Ti}_3(\text{Fe}_{0.5}\text{Cr}_{0.5})\text{O}_{15}$ measured using X-rays of wavelength 0.2038 (\AA) are shown in black markers. The red solid line is the calculated pattern using Rietveld analysis which used $A2_1am$ space group. The vertical bars shown in each panel represent the Bragg peaks allowed in that space group. The inset of (a) shows the (0 1 5) and (0 1 7) reflections which support $A2_1am$ space group. The Y-axis of the inset figure is intensity in 10^5 counts.

replacing the Bi or Cr replacing the Fe positions. A similar trend of reduction in the distortion index was seen in the case of doping of Gd in the Bi site¹⁵.

In fact, three space groups $Fmm2$, $A2_1am$ and $Pnn2$ are reported for $\text{Bi}_5\text{Ti}_3\text{FeO}_{15}$ in the literature. These three space groups have a common subset of reflections hkl such that $h+k$, $h+l$, $k+l = 2n$ where n is an integer. Additional reflections can be used to differentiate between the three space groups. For example, (015) and (017) reflections are present in $A2_1am$ and $Pnn2$ but not in $Fmm2$. Similarly, (107) and (109) are present in $Pnn2$ but not in $A2_1am$. However, these reflections are generally weak in $\text{Bi}_5\text{Ti}_3\text{FeO}_{15}$ (this is the case in our data too) and hence difficult to resolve even in high resolution X-ray or neutron diffraction data. The room temperature crystal structure of $\text{Bi}_5\text{Ti}_3\text{FeO}_{15}$ was reported in $A2_1am$ space group through the analysis of neutron diffraction data. Electron diffraction has been recently used to categorically rule out other space groups and confirm $A2_1am$ as the correct space group of $\text{Bi}_5\text{Ti}_3\text{FeO}_{15}$ ³¹. As can be seen in the inset of Figure 4 (a), the $A2_1am$ space group can be differentiated from the $Fmm2$ from the presence of the reflections (0 1 5) and (0 1 7) in our data. The diffraction data of $\text{Bi}_5\text{Ti}_3\text{FeO}_{15}$

and $(\text{Bi}_4\text{La})\text{Ti}_3\text{FeO}_{15}$ contain the reflections (0 1 5) and (0 1 7), while the Cr-doped composition, $\text{Bi}_5\text{Ti}_3(\text{Fe}_{0.5}\text{Cr}_{0.5})\text{O}_{15}$ does not. Just to test it, we have performed Rietveld analysis of the diffraction pattern of $\text{Bi}_5\text{Ti}_3(\text{Fe}_{0.5}\text{Cr}_{0.5})\text{O}_{15}$ using $Fmm2$. However, we are inclined to assign $A2_1am$ as the most probable space group of $\text{Bi}_5\text{Ti}_3(\text{Fe}_{0.5}\text{Cr}_{0.5})\text{O}_{15}$ following the results of the parent compound and the La-doped version. The absence of (0 1 5)/(0 1 7) reflections could be due to powder averaging of those already weak reflections.

The best refinement results for the three compounds in $A2_1am$ gave agreement factors $R_w = 12\%$ and $\text{GOF} = 1.16$ for $\text{Bi}_5\text{Ti}_3\text{FeO}_{15}$, 11% and 1.97 for $(\text{Bi}_4\text{La})\text{Ti}_3\text{FeO}_{15}$, and 15% and 1.1 for $\text{Bi}_5\text{Ti}_3(\text{Fe}_{0.5}\text{Cr}_{0.5})\text{O}_{15}$. We obtained higher values of GOF for all other space groups tested. The refined atomic parameters of $\text{Bi}_5\text{Ti}_3\text{FeO}_{15}$, $(\text{Bi}_4\text{La})\text{Ti}_3\text{FeO}_{15}$, and $\text{Bi}_5\text{Ti}_3(\text{Fe}_{0.5}\text{Cr}_{0.5})\text{O}_{15}$ are collected in Tables S1-4 in the Supplemental Information (SI). The different bond lengths and bond angles of the three compounds are shown in the SI.

	T_N (K)	θ_{cw} (K)	μ_{eff} (μ_B)
$\text{Bi}_5\text{Ti}_3\text{FeO}_{15}$	n.o.	-3.9(4)	3.2(2)
$\text{Bi}_5\text{Ti}_3(\text{Fe}_{0.5}\text{Cr}_{0.5})\text{O}_{15}$	n.o.	-3.2(2)	4.18(3)
$(\text{Bi}_4\text{La})\text{Ti}_3\text{FeO}_{15}$	n.o.	-4.5(2)	4.8(3)

Table 2 The parameters that characterize the magnetism of the three Aurivillius compounds studied in this work. "n.o." is abbreviation for "not observed".

The local crystal structure of the three Aurivillius compounds were studied using pair distribution function analysis. Pattern fittings were performed on the radial distribution function data derived from total scattering data using the small box approach using PDFgui⁵³. All three compounds fit to the $A2_1am$ space group symmetry, however, no quantitative distinctions were obtained despite obtaining good agreement factors. We encountered marginal differences in the scattering intensities of oxygen relative to heavier Bi and metal atoms resulting in high uncertainties in the peak intensities. This had particular impact on the anisotropic displacement parameters (ADPs) of the O-O peaks. The largest peak observed in the data pertains to Bi-Bi (and Bi/La-Bi/La) bonds, and revealed increased disorder of $(\text{Bi}_4\text{La})\text{Ti}_3\text{FeO}_{15}$ in the respective site, consequently affecting the Bi/La-M bond distances observed at 6.5\AA . A close inspection of the Bi-O and Bi/La-O bonds (3.7\AA and 4.6\AA), showed that the parent compound $\text{Bi}_5\text{Ti}_3\text{FeO}_{15}$ presents less disorder. This can be deduced from the relative peak sharpness and has been observed in compounds with similar Bi-O polyhedra environments^{60,61}. A dampening of the pair distribution peaks at $r \approx 50\text{\AA}$ indicates that the particle size for all compounds in the series have a maximum diameter close to the c -axis of the unit cell. We encourage future studies of the local nuclear and potential magnetic structures using neutron powder diffraction to reduce the uncertainties in the PDF peaks⁶². Such analysis would provide feedback on the metal disorder and vacancies as well as reduced uncertainties in the ADPs given the characteristic nuclear scattering lengths.

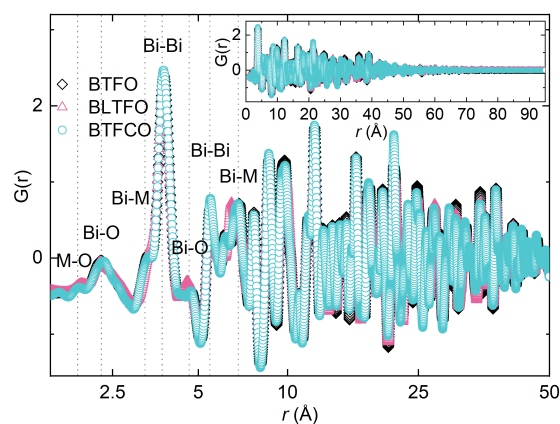


Fig. 5 The radial distribution function $G(r)$ of $\text{Bi}_5\text{Ti}_3\text{FeO}_{15}$, $(\text{Bi}_4\text{La})\text{Ti}_3\text{FeO}_{15}$, and $\text{Bi}_5\text{Ti}_3(\text{Fe}_{0.5}\text{Cr}_{0.5})\text{O}_{15}$ obtained from the X-ray total scattering data from the beamline BXDS at Canadian Light Source. The inset shows the complete data. Different bond lengths are indicated in the main panel.

3.3 Magnetic properties

The magnetic properties, dc magnetic susceptibility $\chi_{\text{dc}}(T)$ and the isothermal magnetization $M(H)$, of the three Aurivillius compounds $\text{Bi}_5\text{Ti}_3\text{FeO}_{15}$, $(\text{Bi}_4\text{La})\text{Ti}_3\text{FeO}_{15}$, and $\text{Bi}_5\text{Ti}_3(\text{Fe}_{0.5}\text{Cr}_{0.5})\text{O}_{15}$ are presented in figure 6 (a), (b) and (c) respectively. In general, a paramagnetic-like nature of the magnetic susceptibility, $\chi_{\text{dc}}(T)$, is seen in all the three compounds where the magnitude of the susceptibility increases as the temperature decreases. Below about 50 K, all the three compounds show a steady increase in the magnitude of magnetic susceptibility. No signature of conventional magnetic phase transitions or anomalies are detected in the temperature dependence of magnetic susceptibility of the three compounds. Figure 6 (a) shows the $\chi_{\text{dc}}(T)$ of $\text{Bi}_5\text{Ti}_3\text{FeO}_{15}$ obtained at an applied field of 5000 Oe. The inset of the figure shows the isothermal magnetization of $\text{Bi}_5\text{Ti}_3\text{FeO}_{15}$ at three different temperatures, 5 K, 20 K and 50 K. Similarly, panels (b) and (c) show the $\chi_{\text{dc}}(T)$ of $(\text{Bi}_4\text{La})\text{Ti}_3\text{FeO}_{15}$ and $\text{Bi}_5\text{Ti}_3(\text{Fe}_{0.5}\text{Cr}_{0.5})\text{O}_{15}$ at applied magnetic fields of 1000 Oe and 5000 Oe respectively. The insets of these figure panels show the magnetization isotherms at different temperatures. Signatures of any kind of field-induced magnetic transitions were absent in the isotherms.

The magnetic susceptibility $\chi_{\text{dc}}(T)$ of the three compounds shown in Figure 6 were analyzed using a modified Curie-Weiss fit, $\chi(T) = \chi_0 + \frac{C}{T - \theta_{\text{cw}}}$. In this equation, χ_0 is a temperature-independent term and θ_{cw} is the Curie-Weiss temperature. The effective moment was computed using the expression, $\mu_{\text{eff}} = \sqrt{8C}\mu_B$ where C is the Curie constant ($C = N_A \mu_{\text{eff}}^2 / 3k_B$), N_A and k_B being the Avogadro's number and Boltzmann constant respectively. The black solid line through the $\chi_{\text{dc}}(T)$ curve in Figure 6 (a-c) is the fit using the modified Curie-Weiss equation given above. The magnetic properties of $\text{Bi}_5\text{Ti}_3\text{FeO}_{15}$ has been reported in the literature by different groups. Our analysis yielded a Curie-Weiss temperature $\theta_{\text{cw}} = -3.9(4)$ K and effective paramagnetic moment $\mu_{\text{eff}} = 3.2(2)$ μ_B . These values are comparable to the reported values, -4.95 K and $3.75(1)$ μ_B ¹⁵. For $(\text{Bi}_4\text{La})\text{Ti}_3\text{FeO}_{15}$, the fit parameters obtained are $\theta_{\text{cw}} = -4.5(2)$ K and $\mu_{\text{eff}} = 4.8(3)$ μ_B .

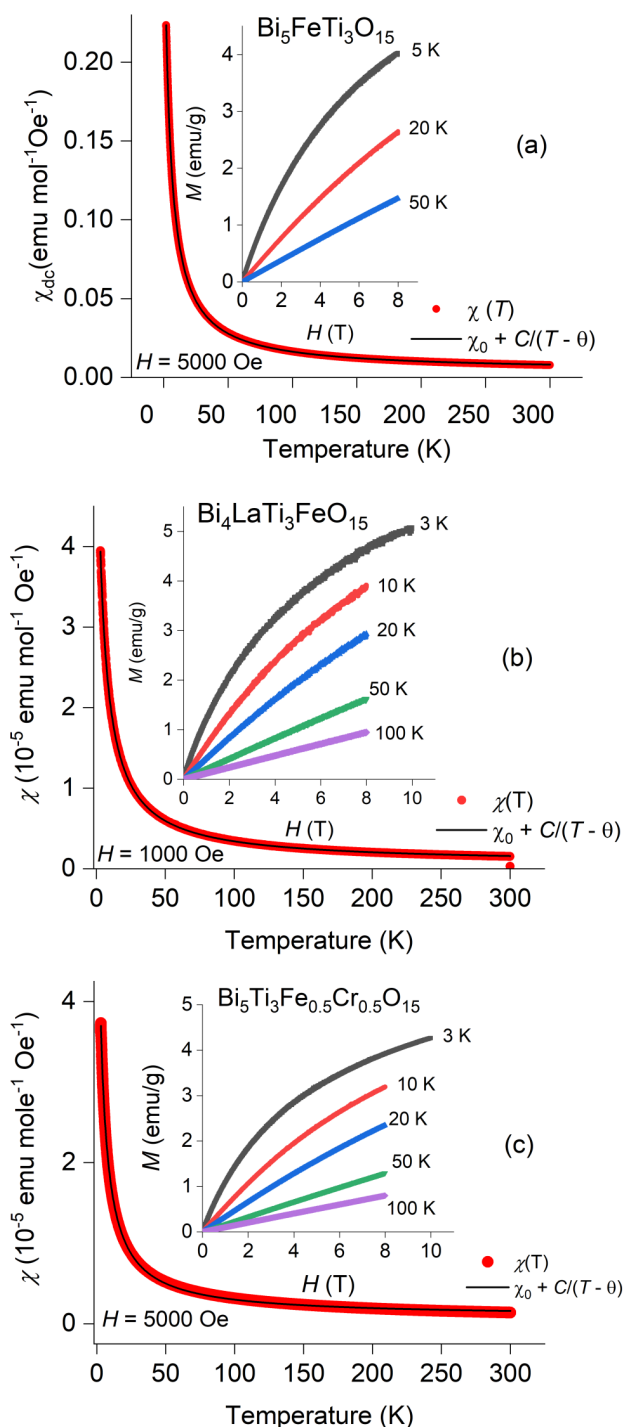


Fig. 6 The magnetic properties of (a) $\text{Bi}_5\text{Ti}_3\text{FeO}_{15}$ (b) $(\text{Bi}_4\text{La})\text{Ti}_3\text{FeO}_{15}$ and (c) $\text{Bi}_5\text{Ti}_3(\text{Fe}_{0.5}\text{Cr}_{0.5})\text{O}_{15}$. The main panels present the magnetic susceptibility $\chi_{\text{dc}}(T)$ (red circles) along with the fit assuming a modified Curie-Weiss law (black line). The inset shows the isothermal magnetization curves, $M(H)$, at different temperatures.

Finally, for $\text{Bi}_5\text{Ti}_3(\text{Fe}_{0.5}\text{Cr}_{0.5})\text{O}_{15}$, the values are $\theta_{\text{cw}} = -3.2(2)$ K and $\mu_{\text{eff}} = 4.18(3) \mu_{\text{B}}$. From our X-ray photoelectron spectroscopy results presented earlier, the oxidation state of Fe in all the three compounds was determined to be +3. In that case, the theoretical spin-only magnetic moment is given by $\mu_{\text{theor.}} = g\mu_{\text{B}}\sqrt{S(S+1)} = 5.92 \mu_{\text{B}}$, where $g = 2$ and $S = 5/2$ for Fe^{3+} . The experimental values that we have obtained from the modified CW fit for the three compounds studied here are less than the theoretical spin-only value of Fe^{3+} . The reduction in the effective paramagnetic moment for our compounds can be explained by the presence of magnetic clusters and oxygen vacancies, which are generally found in Aurivillius compounds⁶³. Due to the low content of Fe in the unit cell, and their random occupation at the B site, long-range magnetic order is not established in BTFO. We know that the Aurivillius structure consists of perovskite layers separated by fluorite-like layers of Bi_2O_2 . Hence, the superexchange interaction between the nearest neighbour Fe ions, Fe-O-Fe is blocked by the fluorite-like layers, leading to predominantly short-range magnetic interactions through a longer exchange path of Fe-O-O-O-Fe. Thus, in the absence of any direct magnetic structure estimation of the BTFO and related compounds in the literature, the magnetism of these compounds is explained in terms of superparamagnetic clusters of Fe. The magnetic properties of Cr-substituted BTFO shows similar magnetic cluster-driven features⁶⁴. The reported value of the effective magnetic moment of $\text{Bi}_5\text{Ti}_3\text{CrO}_{15}$ is $1.92 \mu_{\text{B}}$, which is lower than the spin-only value of Cr^{3+} , $3.87 \mu_{\text{B}}$. The magnetization isotherms of the three compounds presented in the inset of Figure 6 show paramagnetic features at all temperatures other than below 10 K or so. At the lowest temperature of measurement, 3 K, a weak curvature in $M(H)$ is observable, which can be attributed to cooperative magnetic interactions. The parameters extracted from the analysis of magnetic susceptibility of $\text{Bi}_5\text{Ti}_3\text{FeO}_{15}$, $(\text{Bi}_4\text{La})\text{Ti}_3\text{FeO}_{15}$, and $\text{Bi}_5\text{Ti}_3(\text{Fe}_{0.5}\text{Cr}_{0.5})\text{O}_{15}$ are collected in Table 2.

3.4 Specific Heat

The specific heat, $C_p(T)$, of the three Aurivillius compounds $\text{Bi}_5\text{Ti}_3\text{FeO}_{15}$, $(\text{Bi}_4\text{La})\text{Ti}_3\text{FeO}_{15}$, and $\text{Bi}_5\text{Ti}_3(\text{Fe}_{0.5}\text{Cr}_{0.5})\text{O}_{15}$ measured in 0 T magnetic field are shown in Figure 7. Similar to the magnetic susceptibility of these compounds, there is no indication of a phase transition in the temperature range studied here. A rather smooth and monotonic increase of specific heat as a function of increasing temperature is observed in the temperature range 2 K – 250 K. The inset of the panels in Figure 7 shows the variation of the specific heat under external magnetic fields 4 T and 8 T, plotted as C_p/T versus T^2 . Slight upturn in the 0 T specific heat is observed at low temperatures in all three compounds. With the application of external magnetic field, the upturn is suppressed. The low temperature specific heat was analyzed using the following expression, $C_p(T) = aT + bT^3 + cT^5$ in the temperature range 6 K–20 K. The slow upturn in specific heat below 5 K is likely be due to short-range magnetic fluctuations. From the analysis of the low temperature specific heat using the polynomial expansion shown before, a Sommerfeld coefficient of $0.097(8) \text{ J mol}^{-1} \text{ K}^{-1}$ was obtained for $\text{Bi}_5\text{Ti}_3\text{FeO}_{15}$ under 0 T. Correspond-

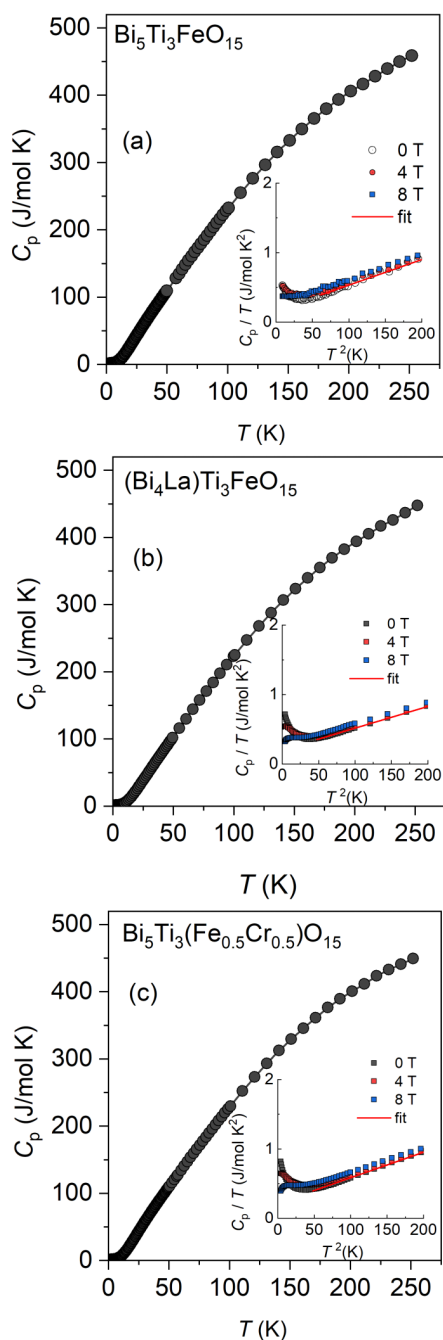


Fig. 7 Specific heat of (a) $\text{Bi}_5\text{Ti}_3\text{FeO}_{15}$, (b) $(\text{Bi}_4\text{La})\text{Ti}_3\text{FeO}_{15}$, and (c) $\text{Bi}_5\text{Ti}_3(\text{Fe}_{0.5}\text{Cr}_{0.5})\text{O}_{15}$. No signature of a phase transition is observed in any of the compounds. The insets show the low temperature part of the specific heat under external magnetic fields, 4 T and 8 T. The red solid line in the inset is a curve fit using the relation, $C_p(T) = aT + bT^3 + cT^5$, where a , b and c are fitting parameters.

ing values for $(\text{Bi}_4\text{La})\text{Ti}_3\text{FeO}_{15}$ and $\text{Bi}_5\text{Ti}_3(\text{Fe}_{0.5}\text{Cr}_{0.5})\text{O}_{15}$ are respectively $0.147(4) \text{ J mol}^{-1} \text{ K}^{-1}$ and $0.174(8) \text{ J mol}^{-1} \text{ K}^{-1}$. The very small values of the Sommerfeld coefficient are in agreement with insulating state of our samples. From the b values, the Debye temperature θ_D can be estimated using the equation, $\theta_D = (\frac{12p\pi^4 R}{5b})^{1/3}$, where p is the number of atoms per formula unit and R is the universal gas constant. Thus, $\theta_D = 213 \text{ K}$ was obtained for $\text{Bi}_5\text{Ti}_3\text{FeO}_{15}$. Corresponding values for $(\text{Bi}_4\text{La})\text{Ti}_3\text{FeO}_{15}$ and $\text{Bi}_5\text{Ti}_3(\text{Fe}_{0.5}\text{Cr}_{0.5})\text{O}_{15}$ are 226 K and 217 K.

3.5 Dielectric properties

In Figure 8 (a), the ferroelectric polarization versus electric field (PE) loop of $\text{Bi}_5\text{Ti}_3\text{FeO}_{15}$ which was recorded within the range of $\pm 100 \text{ kV/cm}$ electric field is shown. Pristine sample of $\text{Bi}_5\text{Ti}_3\text{FeO}_{15}$ did not exhibit saturation upto 100 kV/cm and required a higher electric field to completely polarize the domains. The maximum polarization value reached is $1.56 \mu\text{Ccm}^{-2}$, while the remnant polarization settled around $0.15 \mu\text{Ccm}^{-2}$, and the coercive field measured approximately 9 kV/cm . Figure 8 (b) displays the PE loop of sample $(\text{Bi}_4\text{La})\text{Ti}_3\text{FeO}_{15}$, measured between $\pm 80 \text{ kV}$. The sample doped with La at the Bi site demonstrated an increase in polarization to $2.7 \mu\text{Ccm}^{-2}$ compared to the parent $\text{Bi}_5\text{Ti}_3\text{FeO}_{15}$. Additionally, there is increment in both remnant polarization and coercivity. The PE loop of the $\text{Bi}_5\text{Ti}_3(\text{Fe}_{0.5}\text{Cr}_{0.5})\text{O}_{15}$ could not be measured due to high leakage currents.

Plots of frequency-dependent dielectric constant at various temperatures, $\epsilon'(f, T)$, for $\text{Bi}_5\text{Ti}_3\text{FeO}_{15}$, $(\text{Bi}_4\text{La})\text{Ti}_3\text{FeO}_{15}$, and $\text{Bi}_5\text{Ti}_3(\text{Fe}_{0.5}\text{Cr}_{0.5})\text{O}_{15}$ are shown in Figure 9 (a, b and c). At a given temperature, the dielectric constant is seen to decrease with increasing frequency, which can be attributed to the contributions from grains and grain boundaries. At low frequencies, the primary influence on the dielectric constant comes from grain boundaries. Conversely, at higher frequencies, the dominant contribution stems from the grains. Upon increasing the temperature

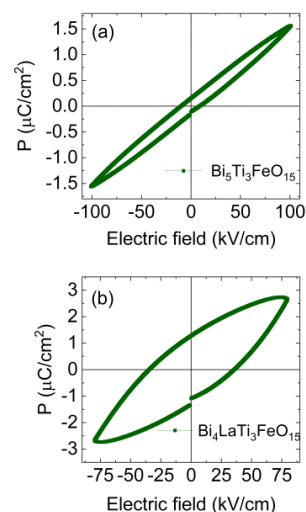


Fig. 8 The ferroelectric loops of (a) $\text{Bi}_5\text{Ti}_3\text{FeO}_{15}$ (b) $(\text{Bi}_4\text{La})\text{Ti}_3\text{FeO}_{15}$. A larger hysteresis loop emerged in $(\text{Bi}_4\text{La})\text{Ti}_3\text{FeO}_{15}$ with La doping. While $\text{Bi}_5\text{Ti}_3(\text{Fe}_{0.5}\text{Cr}_{0.5})\text{O}_{15}$ samples were leaky and hence measuring them was not possible.

while maintaining a constant frequency, the dielectric constant shows an upward shift in the frequency scan plot (Figure 9 (a-c)). This observation indicates that grain boundary contribution becomes more pronounced at lower frequencies with rising temperatures. However, at larger frequencies, the increase in dielectric constant with temperature is comparatively smaller. The decrease in the dielectric constant with increasing frequency is mainly attributable to the diminished contribution from grain boundaries. At lower frequencies with increasing temperature, a significant rise in dielectric constant values indicates a pronounced dielectric dispersion arising from thermally activated charges. At higher temperatures, the charge carriers within grain boundaries become thermally activated, allowing them to move more freely. As a result, the alignment of dipoles with an applied electric field improves, leading to a higher dielectric constant. Similarly, at elevated temperatures, the orientation of dipoles within the grain also improves with the applied electric field, thereby causing an increase in the dielectric constant at higher frequencies. The contribution from grains is relatively smaller.

Frequency versus AC conductivity, $\sigma_{ac}(f, T)$ plots at several temperatures between 305 K and 500 K are shown in Figure 9 (d to f) for all three samples. AC conductivity was calculated using the relation $\sigma_{ac} = \omega \epsilon_0 \epsilon''$ where σ_{ac} is AC conductivity, ω is the angular frequency of the applied AC voltage, ϵ_0 is the permittivity of the free space and ϵ'' imaginary part of the dielectric constant. AC conductivity increases with increasing temperature and frequency. In polycrystalline materials, the resistance of grain boundaries is higher than that of the grains, resulting in lower AC conductivity at smaller frequencies. As mentioned in the dielectric part, at high temperatures, the charge carriers within grain boundaries become thermally activated, allowing them to move more freely, which increases the conductivity with increasing temperature. The increase in conductivity at higher temperatures is more significant at lower frequencies due to the activation of charge carriers at grain boundaries with increasing temperature. La doping in $\text{Bi}_5\text{Ti}_3\text{FeO}_{15}$ leads to a slight decrease in the dielectric constant, while Cr doping at the Fe site leads to a large increment in the dielectric constant. The AC conductivity of the La-doped compound increases slightly. However, a decrease in the AC conductivity was observed in the Nd-doped sample. It was reported that Nd doping decreases the Bi evaporation and the oxygen vacancy creation, increasing the resistivity of the material⁶⁵. The AC conductivity of the Cr-doped sample is an order of magnitude larger than the AC conductivity of the other two samples. Cr evaporation is evident at higher temperatures which gives rise to the creation of oxygen vacancies giving rise to an increase in the AC conductivity. An increase in the dielectric constant of the Cr-doped sample can also be because of oxygen vacancies in the sample. A little increase in the AC conductivity of the La-doped sample with respect to the pristine sample is a bit surprising as La doping is expected to decrease oxygen vacancies.

3.6 Raman scattering

The Raman spectra of the $\text{Bi}_5\text{Ti}_3\text{FeO}_{15}$ compound and its Bi_2O_3 , Fe_2O_3 , and TiO_2 constituents are presented in Figure 10 (a-d), as

labeled. Although structural changes are expected for the oxide constituents during sintering, recording their Raman spectra could provide insights into the complex phonon modes observed for the bismuth iron titanate compound. For example, the most intense feature in the $\text{Bi}_5\text{Ti}_3\text{FeO}_{15}$ spectrum is a convolution of three vibrational lines centered at around 208, 262, and 332 cm^{-1} . The Raman peak at 208 cm^{-1} can be associated with contributions from Bi_2O_3 lines at 184 cm^{-1} and 210 cm^{-1} ^{66,67}, as well as the Fe_2O_3 strong vibration at 217 cm^{-1} ^{68,69}. At a glance, the dominant vibrational line at 262 cm^{-1} could correspond to downshifted peaks at 275 cm^{-1} from Fe_2O_3 and 283 cm^{-1} from Bi_2O_3 . However, TiO_2 exhibits a structural transition from anatase to rutile at temperatures higher than 750°C, such as the one employed in this work. Since the rutile phase has a Raman-active phonon mode at 235 cm^{-1} ⁷⁰, we attribute the 262 cm^{-1} feature to the torsional bending of TiO_6 octahedra, as previously reported^{27,71-73}. An influence from the rutile titania octahedral bending and stretching modes is seen at 332 cm^{-1} , too. The proximity of this vibration to the strong Bi_2O_3 line at 314 cm^{-1} implies an additional contribution from bending modes of distorted BiO_6 subunits. The 547 cm^{-1} and 858 cm^{-1} Raman peaks are correlated with the $(\text{Fe}/\text{Ti})\text{O}_6$ octahedra, respectively^{27,70-73}. The observed vibrations in the spectrum of Fe_2O_3 shown in Figure 10 (d) are consistent with those reported for hematite^{68,69}, with a forbidden Eu Raman mode around 660 cm^{-1} . Thus, we attribute the weak bands at 547 cm^{-1} and 710 cm^{-1} to the torsional bending modes of the FeO_6 octahedron. The latter Raman vibration is specific to iron incorporation into bismuth-layered oxides with titanium-based octahedra⁷³. Another association with rutile titania is at 848 cm^{-1} , which consists of an upshifted vibration from TiO_2 characteristic phonon mode at 826 cm^{-1} ⁷⁰. The Raman vibrations seen in the higher frequency region of the $\text{Bi}_5\text{Ti}_3\text{FeO}_{15}$ spectrum consist of dominant contributions from torsional, bending, and stretching of Ti–O/Fe–O bonds in the corresponding $(\text{Ti}/\text{Fe})\text{O}_6$ octahedra. At lower frequencies, vibrations from the Bi_2O_3 and TiO_2 constituents prevail.

The Raman spectra of $(\text{Bi}_4\text{La})\text{Ti}_3\text{FeO}_{15}$ and $\text{Bi}_5\text{Ti}_3(\text{Fe}_{0.5}\text{Cr}_{0.5})\text{O}_{15}$ compounds, synthesized by co-doping the $\text{Bi}_5\text{Ti}_3\text{FeO}_{15}$ parent compound with La and Cr, are presented in Figure 11 (a) and (b), respectively. For easier detection of the dopant's influence on the $\text{Bi}_5\text{Ti}_3\text{FeO}_{15}$ structure, the spectra of La_2O_3 and Cr_2O_3 are shown, too. A comparison between the $(\text{Bi}_4\text{La})\text{Ti}_3\text{FeO}_{15}$ and $\text{Bi}_5\text{Ti}_3\text{FeO}_{15}$ spectra reveals visible vibrational changes, with new Raman peaks at 418 and 608 cm^{-1} . These peaks could be associated with lanthanum incorporation into the lattice of the parent compound, particularly the 608 cm^{-1} vibrational line, which is present in the La_2O_3 spectrum as well. The well-defined vibrational band at 418 cm^{-1} is attributed tentatively to a downshifted La_2O_3 vibration at 451 cm^{-1} ⁷⁴. Supporting remarks of lanthanum presence are also the features at 218 and 262 cm^{-1} , which could correspond to downshifted La_2O_3 vibrations from 230 and 283 cm^{-1} , respectively. While these observations demonstrate lanthanum incorporation, the weakness of 332 cm^{-1} band and the observed shift from 208 to 218 cm^{-1} confirm a La-cation substitution of Bi in the lattice.

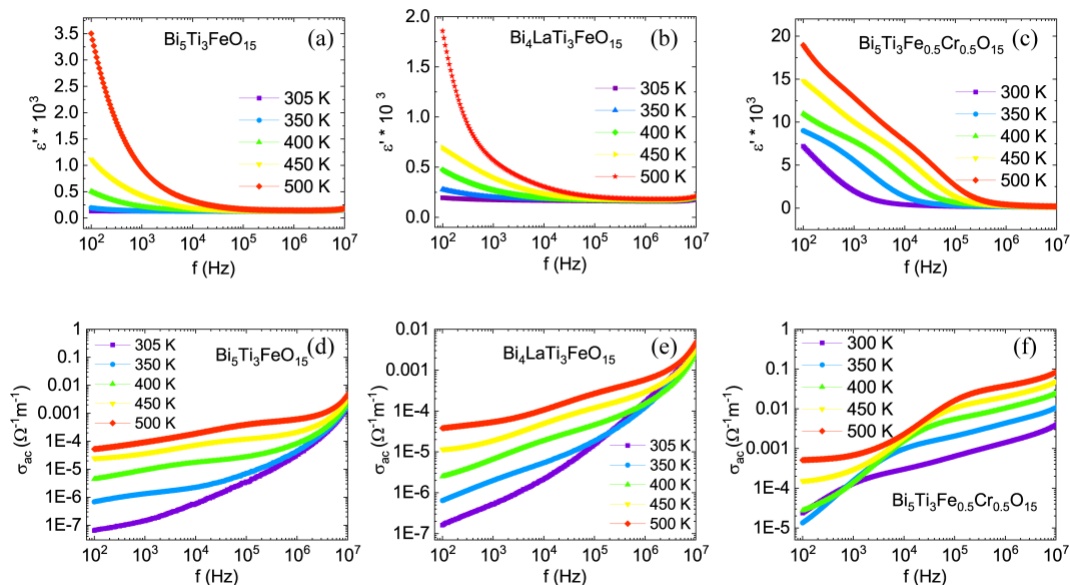


Fig. 9 (a-e) Frequency-dependent dielectric constant ϵ' and AC conductivity σ_{ac} of $\text{Bi}_5\text{Ti}_3\text{FeO}_{15}$, $(\text{Bi}_4\text{La})\text{Ti}_3\text{FeO}_{15}$, and $\text{Bi}_5\text{Ti}_3(\text{Fe}_{0.5}\text{Cr}_{0.5})\text{O}_{15}$ at different temperatures in the range 300–500 K.

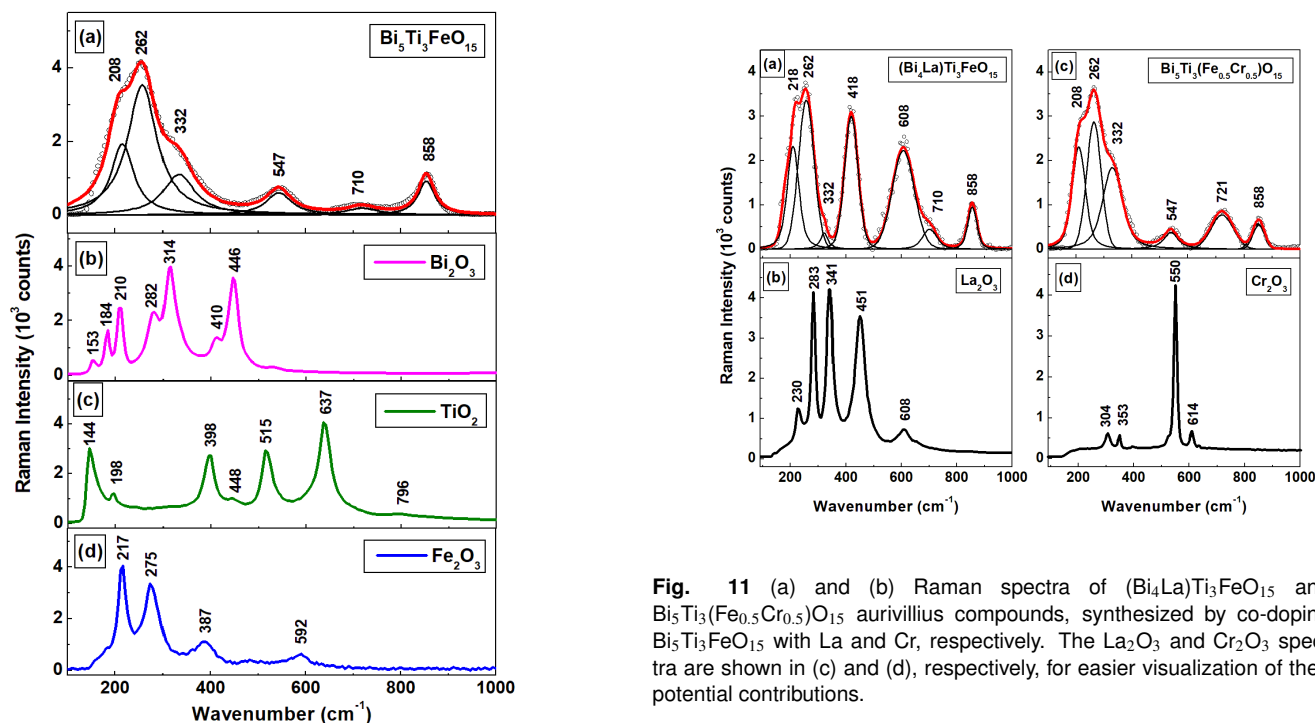


Fig. 10 (a)–(d): Raman spectra of $\text{Bi}_5\text{Ti}_3\text{FeO}_{15}$ compound and its Bi_2O_3 , Fe_2O_3 , and TiO_2 constituents, as labeled.

The fitted 208 and 332 cm^{-1} features seen in the spectrum of $\text{Bi}_5\text{Ti}_3\text{FeO}_{15}$ were associated with contributions from vibrational modes of Bi_2O_3 and distorted BiO_6 and TiO_6 subunits. Variations in the bond lengths with lanthanum incorporation, such as the

Fig. 11 (a) and (b) Raman spectra of $(\text{Bi}_4\text{La})\text{Ti}_3\text{FeO}_{15}$ and $\text{Bi}_5\text{Ti}_3(\text{Fe}_{0.5}\text{Cr}_{0.5})\text{O}_{15}$ aurivillius compounds, synthesized by co-doping $\text{Bi}_5\text{Ti}_3\text{FeO}_{15}$ with La and Cr, respectively. The La_2O_3 and Cr_2O_3 spectra are shown in (c) and (d), respectively, for easier visualization of their potential contributions.

$\text{TiO}_6/\text{FeO}_6$ octahedra previously observed at 547 cm^{-1} , might contribute to the intensity of the 608 cm^{-1} band, especially those from rutile titania. A more intense 710 cm^{-1} vibration than observed for the parent compound supports this remark. There are different structural changes in the Raman spectrum of $\text{Bi}_5\text{Ti}_3(\text{Fe}_{0.5}\text{Cr}_{0.5})\text{O}_{15}$ with Cr-doping. The most noticeable ones are a new Raman band at 721 cm^{-1} and the disappearance

of the 710 cm^{-1} vibration. These observations both correlate with a potential substitution of iron by chromium. Thus, the new 721 cm^{-1} Raman line could be specific for Cr incorporation into the $\text{Bi}_5\text{Ti}_3\text{FeO}_{15}$, as it was the 710 cm^{-1} vibration for Fe. The slightly lower intensity of the 547 cm^{-1} Raman feature, which corresponds to FeO_6 octahedron torsional bending modes, also corroborates with Cr substituting the Fe. The intensity increase for the Raman vibrational line at 332 cm^{-1} infers that Cr incorporation affects the Bi and Ti environments with stronger vibrations from the distorted BiO_6 and TiO_6 subunits. Overall, with La and Cr additions, the significant shifts observed for these aurivillius compounds suggest different effects on the stretching, bending, or torsional behaviour of the oxygen octahedra that are central atoms' dependent.

4 Discussion

In this work, we have studied the bulk physical properties of three Aurivillius perovskite compounds, $\text{Bi}_5\text{Ti}_3\text{FeO}_{15}$, $(\text{Bi}_4\text{La})\text{Ti}_3\text{FeO}_{15}$, and $\text{Bi}_5\text{Ti}_3(\text{Fe}_{0.5}\text{Cr}_{0.5})\text{O}_{15}$. A strong resilience of the Aurivillius structures to chemical and structural modifications is seen through our experimental characterizations of crystal structure, magnetic susceptibility, specific heat and dielectric function. The average crystal structure of the three compounds remain in the orthorhombic $A2_1am$ space group after substituting $\text{Bi}_5\text{Ti}_3\text{FeO}_{15}$ with La or Cr. The ferroelectric Aurivillius phase $\text{Bi}_4\text{Ti}_3\text{O}_{12}$ has large spontaneous polarization and high transition temperatures, ordering into ferroelectric $B2cb$ space group from paraelectric $I4/mmm$ ⁷⁵. A direct method to induce multiferroicity into the lattice of $\text{Bi}_4\text{Ti}_3\text{O}_{12}$ is to dope magnetic atoms in it⁷⁶. Doping Fe in the Aurivillius structure was successful in creating a room temperature multiferroic or magnetoelectric, $\text{Bi}_5\text{Ti}_3\text{FeO}_{15}$ ^{63,77}. The crystal structure of $\text{Bi}_5\text{Ti}_3\text{FeO}_{15}$ was reported as $Fmm2$ using X-ray studies²⁸ and later as $A2_1am$ using neutron diffraction studies²⁹. The ferroelectric Curie temperature for $\text{Bi}_5\text{Ti}_3\text{FeO}_{15}$ has been reported in a large range of 885 K – 1075 K by different groups^{18,28}. Different magnetic ground states are reported for $\text{Bi}_5\text{Ti}_3\text{FeO}_{15}$ in the literature, from weak ferromagnetism at room temperature⁷⁸ to G-type antiferromagnetism with a transition temperature of 80 K⁷⁹. The variations in crystal structure and magnetic properties seen reported in the literature are mainly due to synthesis conditions, annealing and processing methods. In the present work, our structural studies reveal that the space group is $A2_1am$ for $\text{Bi}_5\text{Ti}_3\text{FeO}_{15}$, $(\text{Bi}_4\text{La})\text{Ti}_3\text{FeO}_{15}$, and $\text{Bi}_5\text{Ti}_3(\text{Fe}_{0.5}\text{Cr}_{0.5})\text{O}_{15}$. Moreover, no magnetic phase transition is observed in the studied temperature range of 2 K–300 K; only a paramagnetic-like response is obtained. The effective paramagnetic moment determined from Curie-Weiss fit to the inverse magnetic susceptibility yielded comparable values for the three compounds. From X-ray photoelectron spectroscopy we determined the oxidation states of the cations in the three compounds to be Bi(III), Fe(III) and Cr(III). The magnetic moment values we have obtained for $\text{Bi}_5\text{Ti}_3\text{FeO}_{15}$, $(\text{Bi}_4\text{La})\text{Ti}_3\text{FeO}_{15}$, and $\text{Bi}_5\text{Ti}_3(\text{Fe}_{0.5}\text{Cr}_{0.5})\text{O}_{15}$ are comparable to the theoretical values of Fe(III)/Cr(III) species. The strength of the antiferromagnetic correlations, as evident from the Curie-Weiss temperatures, are comparable for the three compounds. The absence of any type of

phase transition is reflected in the specific heat data also. However, an upturn in specific heat at low-temperatures, below 5 K, is observed which is likely due to increasing magnetic fluctuations as the temperature is lowered. With increasing externally applied magnetic fields, the upturn in specific heat is suppressed.

While the bulk crystal structure, magnetism and specific heat do not differentiate the physical properties of $\text{Bi}_5\text{Ti}_3\text{FeO}_{15}$, $(\text{Bi}_4\text{La})\text{Ti}_3\text{FeO}_{15}$, and $\text{Bi}_5\text{Ti}_3(\text{Fe}_{0.5}\text{Cr}_{0.5})\text{O}_{15}$, a local probe like Raman scattering shows signatures of bond stretching, bending or torsional effects due to the introduction of La or Cr into the lattice of $\text{Bi}_5\text{Ti}_3\text{FeO}_{15}$. The electric polarization is the only bulk physical property that shows a change as a result of the chemical doping. With La-doping, the PE loop in $(\text{Bi}_4\text{La})\text{Ti}_3\text{FeO}_{15}$ is significantly wider compared to that of $\text{Bi}_5\text{Ti}_3\text{FeO}_{15}$. Earlier works point toward how doping rare earths into the Aurivillius lattice may help to reduce the leakage current and oxygen vacancies, thereby enhancing the ferroelectric response^{80,81}. However, with transition metal doping at the Fe-site, the leakage current in $\text{Bi}_5\text{Ti}_3(\text{Fe}_{0.5}\text{Cr}_{0.5})\text{O}_{15}$ was high and a measurement of PE loop was not possible.

5 Conclusions

The resilience of the Aurivillius structure to chemical doping is demonstrated through our work on three compounds, $\text{Bi}_5\text{Ti}_3\text{FeO}_{15}$, $(\text{Bi}_4\text{La})\text{Ti}_3\text{FeO}_{15}$, and $\text{Bi}_5\text{Ti}_3(\text{Fe}_{0.5}\text{Cr}_{0.5})\text{O}_{15}$. These three compounds crystallize in $A2_1am$ space group at room temperature. They did not show any signs of a phase transition in the temperature range of 2 K–300 K, as deduced from our magnetic susceptibility and specific heat studies. Indications of antiferromagnetic spin fluctuations at low temperatures were obtained from the magnetic susceptibility experiments. The spin fluctuations are suppressed with the application of external magnetic fields. The specific heat data on the three compounds also showed that the low temperature upturn, likely due to the magnetic correlations, is suppressed with the application of external magnetic field. With La-doping, the ferroelectric hysteresis loop of $(\text{Bi}_4\text{La})\text{Ti}_3\text{FeO}_{15}$ is wider than that of the parent, $\text{Bi}_5\text{Ti}_3\text{FeO}_{15}$. We observe changes in the local crystal structure upon La and Cr doping, through Raman scattering and X-ray pair distribution function analysis.

Conflicts of interest

There are no conflicts to declare.

Acknowledgments

KG acknowledges support from the Division of Materials Science and Engineering, Office of Basic Energy Sciences, Office of Science of the U. S. Department of Energy (U.S. DOE). VB acknowledges the support from Idaho National Laboratory's Laboratory Directed Research and Development (LDRD) program under DOE Idaho Operations Office Contract DE-AC07-05ID14517. HSN acknowledges the use of X-ray core facility at UTEP. Part of the research described in this paper was performed using beamline BXDS at the Canadian Light Source, a national research facility of the University of Saskatchewan, which is supported by the Canada Foundation for Innovation (CFI), the Natural Sciences

and Engineering Research Council (NSERC), the National Research Council (NRC), the Canadian Institutes of Health Research (CIHR), the Government of Saskatchewan, and the University of Saskatchewan.

Notes and references

- 1 S.-W. Cheong and M. Mostovoy, *Nature Materials*, 2007, **6**, 13–20.
- 2 N. A. Spaldin and M. Fiebig, *Science*, 2005, **309**, 391–392.
- 3 N. A. Spaldin and R. Ramesh, *Nature Materials*, 2019, **18**, 203–212.
- 4 D. I. Khomskii, *Journal of Magnetism and Magnetic Materials*, 2006, **306**, 1–8.
- 5 K. F. Wang, J. M. Liu and Z. F. Ren, *Advances in Physics*, 2009, **58**, 321–448.
- 6 J. Wu, Z. Fan, D. Xiao, J. Zhu and J. Wang, *Progress in Materials Science*, 2016, **84**, 335–402.
- 7 S. Sun and X. Yin, *Crystals*, 2020, **11**, 23.
- 8 B. Aurivillius, *Arkiv kemi*, 1949, **1**, 463–480.
- 9 T. Takenaka and K. Sakata, *Japanese Journal of Applied Physics*, 1980, **19**, 31.
- 10 H. Sun, X. Lu, J. Su, T. Xu, C. Ju, F. Huang and J. Zhu, *Journal of Physics D: Applied Physics*, 2012, **45**, 385001.
- 11 M. Wu, Z. Tian, S. Yuan and Z. Huang, *Materials Letters*, 2012, **68**, 190–192.
- 12 W. Bai, Y. Gao, J. Zhu, X. Meng, T. Lin, J. Yang, Z. Zhu and J. Chu, *Journal of Applied Physics*, 2011, **109**, 064901.
- 13 T. Jardiell, A. C. Caballero and M. Villegas, *J. Ceram. Soc. Japan*, 2008, **116**, 511–518.
- 14 K. R. Kendall, C. Navas, J. K. Thomas and H.-C. zur Loye, *Chem. Mater.*, 1996, **8**, 642–649.
- 15 V. Koval, I. Skorvanek, G. Viola, M. Zhang, C. Jia and H. Yan, *J. Phys. Chem. C*, 2018, **122**, 15733–15743.
- 16 X. Zuo, E. He, J. Bai, S. Zhu, X. Kan, Z. Hui, J. Yang, X. Zhu and J. Dai, *Current Applied Physics*, 2019, **19**, 1391–1398.
- 17 A. Srinivas, M. M. Kumar, S. V. Suryanarayana and T. Bhimasankaram, *Materials Research Bulletin*, 1999, **34**, 989–996.
- 18 N. A. Lomanova, M. I. Morozov, V. L. Ugolkov and V. V. Gusarov, *Inorg Mater*, 2006, **42**, 189–195.
- 19 H. Sun, X. Lu, T. Xu, J. Su, Y. Jin, C. Ju, F. Huang and J. Zhu, *Journal of Applied Physics*, 2012, **111**, 124116.
- 20 X. Mao, W. Wang, H. Sun, Y. Lu and X. Chen, *Journal of Materials Science*, 2012, **47**, 2960–2965.
- 21 X. Mao, W. Wang, X. Chen and Y. Lu, *Applied Physics Letters*, 2009, **95**, 082901.
- 22 T. Pikula, J. Dzik, P. Guzdek, V. I. Mitsuik, Z. Surowiec, R. Panek and E. Jartych, *Ceramics International*, 2017, **43**, year.
- 23 R. S. Singh, T. Bhimasankaram, G. S. Kumar and S. V. Suryanarayana, *Solid State Communications*, 1994, **91**, year.
- 24 Y. Zhao, H. Fan, G. Liu, Z. Liu and X. Ren, *Journal of Alloys and Compounds*, 2016, **675**, year.
- 25 X. Zuo, S. Zhu, J. Bai, E. He, Z. Hui, P. Zhang, D. Song, W. Song, J. Yang, X. Zhu and J. Dai, *Ceramics International*, 2019, **45**, 137–143.
- 26 L. Cao, Z. Ding, X. Liu, J. Ren, Y. Chen, M. Ouyang, X. Chen and F. Yang, *Journal of Alloys and Compounds*, 2019, **800**, year.
- 27 S. Kooriyattil, R. K. Katiyar, S. P. Pavunny, G. Morell and R. S. Katiyar, *Applied Physics Letters*, 2014, **105**, year.
- 28 F. Kubel and H. Schmid, *Ferroelectrics*, 1992, **129**, year.
- 29 C. H. Hervoches, A. Snedden, R. Riggs, S. H. Kilcoyne, P. Manuel and P. Lightfoot, *Journal of Solid State Chemistry*, 2002, **164**, 280–291.
- 30 C. Chen, K. Song, W. Bai, J. Yang, Y. Zhang, P. Xiang, M. Qin, X. Tang and J. Chu, *Journal of Applied Physics*, 2016, **120**, year.
- 31 Y. Zheng, X. Wu, Y. Zhang, W. Shao and W. Ye, *Acta Crystallographica Section C: Structural Chemistry*, 2020, **76**, 454–457.
- 32 J.-B. Li, Y. P. Huang, G. H. Rao, G. Y. Liu, J. Luo, J. R. Chen and J. K. Liang, *Appl. Phys. Lett.*, 2010, **96**, 222903.
- 33 A. Snedden, C. H. Hervoches and P. Lightfoot, *Physical Review B*, 2003, **67**, year.
- 34 Z. Yu, B. Yu, Y. Liu, P. Zhou, J. Jiang, K. Liang, Y. Lu, H. Sun, X. Chen, Z. Ma et al., *Ceramics International*, 2017, **43**, 14996–15001.
- 35 X. Zuo, S. Zhu, J. Bai, E. He, Z. Hui, P. Zhang, D. Song, W. Song, J. Yang, X. Zhu et al., *Ceramics International*, 2019, **45**, 137–143.
- 36 X. Chen, J. Xiao, Y. Xue, X. Zeng, F. Yang and P. Su, *Ceramics International*, 2014, **40**, 2635–2639.
- 37 Z. Li, K. Tao, J. Ma, Z. Gao, V. Koval, C. Jiang, G. Viola, H. Zhang, A. Mahajan, J. Cao, M. Cain, I. Abrahams, C. Nan, C. Jia and H. Yan, *J. Mater. Chem. C*, 2018, **6**, 2733–2740.
- 38 A. Faraz, T. Maity, M. Schmidt, N. Deepak, S. Roy, M. E. Pemble, R. W. Whatmore and L. Keeney, *J. Am. Ceram. Soc.*, 2017, **100**, 975–987.
- 39 L. Su, X. Lu, L. Chen, Y. Wang, G. Yuan and J. M. Liu, *ACS Applied Materials & Interfaces*, 2018, **10**, 21428–21433.
- 40 B. H. Park, B. S. Kang, S. D. Bu, T. W. Noh, J. Lee and W. Jo, *Nature*, 1999, **401**, 682–684.
- 41 B. B. Yang, M. Y. Guo, D. P. Song, X. W. Tang, R. H. Wei, L. Hu, J. Yang, W. H. Song, J. M. Dai, X. J. Lou, X. B. Zhu and Y. P. Sun, *Applied Physics Letters*, 2017, **111**, year.
- 42 Z. Pan, P. Wang, X. Hou, L. Yao, G. Zhang, J. Wang, J. Liu, M. Shen, Y. Zhang, S. Jiang, J. Zhai and Q. Wang, *Advanced Energy Materials*, 2020, **10**, 2001536.
- 43 D. P. Song, J. Yang, J. X. Sun, L. Y. Chen, Y. Q. Chu, Y. Wang and J. K. Lee, *Journal of Applied Physics*, 2020, **127**, year.
- 44 D. P. Song, J. Yang, B. B. Yang, Y. Wang, L. Y. Chen, F. Wang and X. B. Zhu, *Journal of Applied Physics*, 2019, **125**, year.
- 45 A.-K. Axelsson, F. Le Goupil, M. Valant and N. M. Alford, *Acta Materialia*, 2017, **124**, 120–126.
- 46 S. Hajra, M. Sahu, D. Oh and H. J. Kim, *Ceramics International*, 2021, **47**, 15695–15702.
- 47 J. Chen, Z. Tang, B. Yang and S. Zhao, *Applied Physics Letters*, 2018, **113**, year.
- 48 J. Li, Z. Li, J. He, Y. Hou, Y. Su, L. Qiao and Y. Bai, *physica*

- status solidi (RRL)*–*Rapid Research Letters*, 2021, **15**, 2100251.
- 49 H. Zhang, T. Wei, Q. Zhang, W. Ma, P. Fan, D. Salamon, S.-T. Zhang, B. Nan, H. Tan and Z.-G. Ye, *Journal of Materials Chemistry C*, 2020, **8**, 16648–16667.
- 50 C. B. Muratov, *Physical Review E*, 2002, **66**, 066108.
- 51 V. Vixninin, R. Blinc and R. Pirc, *Ferroelectrics*, 2000, **240**, 1621–1628.
- 52 B. H. Toby and R. B. Von Dreele, *Journal of Applied Crystallography*, 2013, **46**, 544–549.
- 53 C. L. Farrow, P. Juhas, J. W. Liu, D. Bryndin, E. S. Božin, J. Bloch, T. Proffen and S. J. L. Billinge, *Journal of Physics: Condensed Matter*, 2007, **19**, 335219.
- 54 J. A. Dias, R. E. S. Bretas, L. M. S. Marcondes and M. R. Morelli, *Journal of Materials Science: Materials in Electronics*, 2019, **30**, 16812–16820.
- 55 N. Kocoń, J. Dzik, D. Szalbot, T. Pikula, M. Adamczyk-Habrajska and B. Wodecka-Duś, *Archives of Metallurgy and Materials*, 2021, **66**, 359.
- 56 L. Li, H. Yuan, P. Huang, Y. Zhang, L. Sheng, P. Zheng, L. Zhang, F. Wen, W. Wu and Z. Xu, *Ceramics International*, 2020, **46**, 2178–2184.
- 57 M. Kindelmann, K. Ran, W. Rheinheimer, K. Morita, J. Mayer, M. Bram and O. Guillon, *Journal of the American Ceramic Society*, 2021, **104**, 4946–4959.
- 58 G. L. McPherson, W. M. Heung and J. J. Barraza, *Journal of American Chemical Society*, 1978, **100**, 469.
- 59 H. M. Rietveld, *Journal of Applied Crystallography*, 1969, **2**, 65–71.
- 60 Y. Yoneda, S. Kohara, S. Hamazaki, M. Takashige *et al.*, *Nuclear Instruments and Methods in Physics Research Section B: Beam Interactions with Materials and Atoms*, 2005, **238**, 150–153.
- 61 D. Maurya, A. Charkhesht, S. K. Nayak, F.-C. Sun, D. George, A. Pramanick, M.-G. Kang, H.-C. Song, M. M. Alexander, D. Lou *et al.*, *Physical Review B*, 2017, **96**, 134114.
- 62 S. Zhang, J. Gong, D. Z. Xiao, B. R. Jayan and A. J. McGaughey, *Computational Materials Science*, 2023, **218**, 111964.
- 63 H. Zhao, H. Kimura, Z. Cheng, M. Osada, J. Wang, X. Wang, S. Dou, Y. Liu, J. Yu, T. Matsumoto *et al.*, *Scientific Reports*, 2014, **4**, 5255.
- 64 J. Liu, W. Bai, J. Yang, W. Xu, Y. Zhang, T. Lin, X. Meng, C.-G. Duan, X. Tang and J. Chu, *Journal of Applied Physics*, 2013, **114**, 234101.
- 65 F. Rehman, H.-B. Jin, L. Wang, A. Tanver, D.-Z. Su and J.-B. Li, *RSC Advances*, 2016, **6**, 21254–21260.
- 66 A. L. J. Pereira, O. Gomis, J. A. Sans, J. Pellicer-Porres, F. J. Manjón, A. Beltran, P. Rodríguez-Hernández and A. Muñoz, *Journal of Physics: Condensed Matter*, 2014, **26**, 225401.
- 67 B. Ling, X. W. Sun, J. L. Zhao, Y. Shen, Z. L. Dong, L. Sun, S. Li and S. Zhang, *Journal of Nanoscience and Nanotechnology*, 2010, **10**, 8322–8327.
- 68 A. M. Jubb and H. C. Allen, *ACS Applied Materials & Interfaces*, 2010, **2**, 2804–2812.
- 69 A. Sunny, A. Thirumurugan and K. Balasubramanian, *Physical Chemistry Chemical Physics*, 2020, **22**, 2001–2009.
- 70 U. Balachandran and N. G. Eror, *Journal of Solid State Chemistry*, 1982, **42**, 276–282.
- 71 P. P. Jiang, Z. H. Duan, L. P. Xu, X. L. Zhang, Y. W. Li, Z. G. Hu and J. H. Chu, *Journal of Applied Physics*, 2014, **115**, year.
- 72 H. Zhang, H. Ke, P. Ying, H. Luo, L. Zhang, W. Wang, D. Jia and Y. Zhou, *Journal of Sol-Gel Science and Technology*, 2018, **85**, 132–139.
- 73 W. C. Ferreira, G. L. C. Rodrigues, B. S. Araújo, F. A. A. de Aguiar, A. N. A. de Abreu Silva, P. B. A. Fachine, C. W. de Araujo Paschoal and A. P. Ayala, *Ceramics International*, 2020, **46**, 18056–18062.
- 74 S. I. Boldish and W. B. White, *Spectrochimica Acta Part A: Molecular Spectroscopy*, 1979, **35**, 1235–1242.
- 75 R. E. Newnham, J. J. Kramer, W. A. Schulze and L. E. Cross, *Journal of Applied Physics*, 1978, **49**, 6088–6091.
- 76 L. Keeney, C. Downing, M. Schmidt, M. E. Pemble, V. Nicolosi and R. W. Whatmore, *Scientific Reports*, 2017, **7**, 1737.
- 77 A. Y. Birenbaum and C. Ederer, *Phys. Rev. B*, 2014, **90**, 214109.
- 78 X. Y. Mao, W. Wang and X. B. Chen, *Solid State Communications*, 2008, **147**, 186–189.
- 79 A. Srinivas, S. V. Suryanarayana, G. S. Kumar and M. M. Kumar, *Journal of Physics: Condensed Matter*, 1999, **11**, 3335.
- 80 J. Paul, S. Bhardwaj, K. K. Sharma, R. K. Kotnala and R. Kumar, *Journal of Alloys and Compounds*, 2015, **634**, 58–64.
- 81 C. Long, H. Fan and M. Li, *Dalton Trans.*, 2013, **42**, 3561.